Accurate PMU Frequency and ROCOF Tracking via IpQPFT: A Novel Interpolated QPFT Framework

Cesar Cazal, *Graduate Student Member, IEEE*, Guglielmo Frigo, *Senior Member, IEEE*, Ian Andrés Morales Sandoval, Ferdinanda Ponci, *Senior Member, IEEE*, and Antonello Monti, *Senior Member, IEEE*

***Abstract*—Reliable rate of change of frequency (ROCOF) estimation is critical for phasor measurement unit (PMU)-based monitoring, protection, and control, yet the conventional finite-difference formulation remains inadequate under rapidly varying grid conditions. This article proposes an interpolated quadratic-phase Fourier transform (IpQPFT), which extends the recently introduced quadratic phase Fourier transform (QPFT) through bi-dimensional polynomial interpolation and a multivariate Newton–Raphson (NR) procedure, enabling accurate real-time ROCOF estimation while preserving compatibility with the interpolated discrete Fourier transform (IpDFT) family. The proposed method is assessed according to IEEE/IEC 60255-118-1:2018 and benchmarked against the compressive sensing Taylor–Fourier multifrequency (CSTFM) and total least squares estimation of signal parameters via rotational invariance (TLS-ESPRIT) methods. The results show that the IpQPFT preserves the favorable behavior of discrete Fourier transform (DFT)-interpolation techniques under static and quasi-static conditions, while providing a more physically consistent response under genuine frequency-ramp scenarios, where ROCOF is identified directly within the signal model. Moreover, the method achieves compliant performance in the main static and dynamic tests, with reduced ramp-test error and low variability under harmonic distortion (HD), whereas the AM and PM results evidence the expected tradeoff between modulation tracking capability and observation-window length. Finally, a real-world analysis of the 2015 Turkey blackout confirms the ability of the proposed estimator to track dynamic ROCOF evolution and to resolve sharp transitions associated with major disturbance events. Overall, the IpQPFT constitutes a practical ROCOF-aware enhancement of DFT-based synchrophasor estimation for non-stationary power-system conditions.**

***Index Terms*—Discrete Fourier transform (DFT), interpolation techniques, non-linear optimization, rate of change of frequency (ROCOF).**

Received 28 November 2025; revised 20 May 2026; accepted 21 June 2026. Date of publication 14 July 2026; date of current version 27 July 2026. This work was supported by the InterSCADA Project (Interoperable, Scalable, and Secure AC-DC Modular Automation System), funded by the European Union's Horizon Europe Program under Grant 101173007. The Associate Editor coordinating the review process was Dr. Valentina Cosentino. *(Corresponding author: Cesar Cazal.)*

Cesar Cazal, Ian Andrés Morales Sandoval, and Ferdinanda Ponci are with the Institute for Automation of Complex Power Systems, RWTH Aachen University, 52074 Aachen, Germany (e-mail: cesar.cazal@eonerc.rwth-aachen.de; fponci@eonerc.rwth-aachen.de).

Guglielmo Frigo is with the Federal Institute of Metrology, METAS, CH-3003 Bern, Switzerland (e-mail: guglielmo.frigo@metas.ch).

Antonello Monti is with the Institute for Automation of Complex Power Systems, RWTH Aachen University, 52074 Aachen, Germany, and also with the Centre for Digital Energy, Fraunhofer FIT, 53757 Aachen, Germany (e-mail: amonti@eonerc.rwth-aachen.de).

Digital Object Identifier 10.1109/TIM.2026.3712977

I. Introduction

IN MANY Phasor measurement unit (PMU)-based applications, the rate of change of frequency (ROCOF) is traditionally approximated by differencing two consecutive frequency estimates. Although computationally simple, this approach presents fundamental limitations for real-time monitoring, protection, and control. By contrast, dynamic ROCOF estimates derived from model-based algorithms, such as the Taylor–Fourier method, offer significant advantages from the application perspective.

Dynamic ROCOF enables faster and more reliable detection of genuine frequency ramps (FRs). Model-based estimators measure the instantaneous curvature of the phase trajectory within the estimation window, allowing earlier and more accurate identification of generator outages, islanding events, or severe load–generation imbalances, while exhibiting substantially lower noise sensitivity. This condition severely degrades the dependability of ROCOF relays, under-frequency load shedding schemes, and inverter-based resource controls, considering dynamic ROCOF conditions necessary for accurate inertia estimation [1]. For the estimation of fundamental frequency and, by extension, ROCOF, the primary reference governing performance criteria and test requirements is IEEE/IEC 60255-118-1:2018 [2] (from now on referred to as the PMU standard).

As summarized in [3], existing algorithms can be broadly grouped into four principal categories. The first category comprises filter-bank or cascaded-filter techniques [4], [5], which extract frequency information through tailored filtering structures. A second group includes interpolated discrete Fourier transform (IpDFT) methods equipped with leakage compensation mechanisms [6]. A third family is formed by techniques exploiting Taylor-series expansions of the underlying signal model [7]. Finally, a fourth class consists of approaches based on functional projections or nonlinear parametric fitting [8]. Additional strategies have been proposed to address specific measurement challenges, such as ROCOF estimation under broad or continuous spectral conditions [9] and approaches that exploit dictionary-based mappings for characterizing abrupt events [10]. Among all previously cited methods, two have recently gained particular prominence due to their favorable metrological properties and demonstrated compliance with the PMU standard [11]. The first is the class of Taylor-series estimators for dynamic synchrophasor measurement, where ROCOF is obtained directly from the second-order phase expansion. The second is the group of discrete Fourier transform (DFT)-based estimators, most notably the IpDFT method, which is used for static synchrophasor computation; in this case, ROCOF is commonly derived using finite-difference operations on successive frequency estimates. Hybrid techniques have also been reported, where a Taylor-series expansion of the IpDFT model is solved via weighted least squares.

More recently, parametric subspace-based approaches have also shown promising performance for dynamic PMU applications. In particular, the second-order Taylor-series-approximated total least squares estimation of signal parameters via the rotational invariance (TLS-ESPRIT) method proposed in [12] estimates the phasor together with the first and second derivatives of amplitude and phase from a single data window, incorporating model-order estimation tailored to M-class requirements, at the expense of a high computational cost.

Motivated by these limitations, the DFT formulation explicitly incorporating ROCOF dynamics has been adopted in [13]. This method, from which the current study represents an extension, can be interpreted as a specific instance of the quadratic phase Fourier transform (QPFT) originally formalized in [14] and [15]. Moreover, the work in [13] evaluated the inherent ROCOF limitations of the IpDFT, identifying the main contributors to estimation error under dynamic conditions, and proposed a modification of the DFT kernel that embeds ROCOF directly into the transform, evidencing the quasi-stationary properties of common DFT-based techniques. While the extended DFT formulation used in [13] demonstrated promising results under dynamic ROCOF conditions, important limitations have been discussed to reach a minimum maturity level for its implementation in PMUs. As an example, we are not aware of any interpolated QPFT method in the literature that makes real-time applications possible. Moreover, with the introduction of a new axis in the ROCOF domain, the effect of window functions along this axis remains unknown. In this context, numerical methods have proven effective for DFT interpolation when closed-form solutions are unavailable, as discussed in [16].

To address these limitations, this work proposes an interpolated quadratic-phase Fourier transform (IpQPFT) procedure for the ROCOF-DFT, based on polynomial interpolation and the multivariate Newton–Raphson (NR) method, making the algorithm suitable for real-time PMU applications. The proposed method is evaluated against the PMU standard, and compared with the compressive sensing Taylor–Fourier multifrequency (CSTFM) [17] and the TLS-ESPRIT method [12]. Finally, the various methods are evaluated in a real-world case study derived from the 2015 Turkey power outage [11].

Summarizing, the main contributions of this study are as follows.

1) The formulation of a practical IpQPFT algorithm for the ROCOF-DFT, based on bi-dimensional polynomial interpolation and a multivariate NR procedure, enabling real-time synchrophasor estimation.
2) The demonstration that the proposed estimator operates as a ROCOF-aware extension of the IpDFT family, preserving compatibility with conventional DFT-interpolation procedures, including peak-location and leakage-mitigation stages, while retaining IpDFT-like accuracy under static and quasi-static conditions.
3) The assessment of the algorithm's accuracy and performance according to the IEC/IEEE 60255-118-1:2018 standard, with benchmarking and validation against the CSTFM, and TLS-ESPRIT methods using a real-world case study based on the 2015 Turkey power outage.

II. Theoretical Background

In this section, a summary of the ROCOF-DFT method proposed in [13] is presented. Furthermore, the interpolation algorithm from [16], as well as the theoretical assumptions for a multivariate interpolation approach, are presented.

A. Rocof-Dft Fundamentals

In [13], a new formulation of the DFT has been proposed to address dynamic conditions introduced by the effects of ROCOF, modifying the Fourier kernel with the introduction of a separate ROCOF axis. This modification breaks the quasi-stationary frequency assumption by imposing

$$\frac{dR}{dt} = 0 \tag{1}$$

where "R" is the ROCOF over time, leading to the following expressions for the instantaneous frequency and phase solutions for (1), respectively,

$$f(t) = f_0 + R \cdot t \tag{2}$$

$$\phi(t) = \phi_0 + f_0 \cdot t + \frac{1}{2} \cdot R \cdot t^2. \tag{3}$$

Both conditions extend the analysis beyond the quasi-stationary frequency regime, in accordance with the PMU standard. Based on (3), the classical DFT formula can be adapted to adopt the ROCOF contribution, as in [13]

$$X[k, r] = \sum_{n=0}^{N-1} x[n] \cdot e^{-j\frac{2\pi \cdot k \cdot n}{N}} \cdot e^{-j\frac{\pi \cdot r \cdot n^2}{N \cdot F_s}} \tag{4}$$

where $X[k, r]$ is the new complex result of the ROCOF-DFT, with "k," and "r" the frequency and ROCOF bins, respectively. Moreover, "N" is the number of samples processed within the observation window, while "n" is the current sample processed, with "F_s" as the sampling frequency applied. In this scenario, the classical DFT formulation inherently assumes a zero ROCOF, as does the IpDFT by extension. Consequently, any non-zero ROCOF perturbs the estimation process and introduces errors when present. Additionally, the inclusion of ROCOF as a separate axis imposes a 3-D representation for magnitude, frequency, and ROCOF.

B. VM Interpolation Method

As noted in [16], conventional closed-form solutions are restricted to only a few window functions, with the Hann window being one of the few practical cases. However, when no closed-form solution exists, when fundamental assumptions

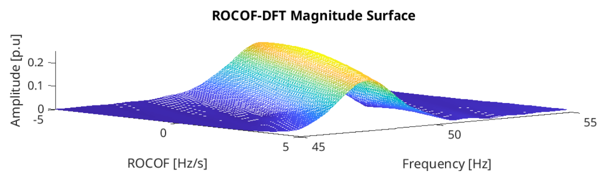

Fig. 1. Hann windowed ROCOF-DFT magnitude surface plot of a signal. It can be appreciated that the local "magnitude tube" surface, formed by the main ROCOF-frequency mode.

are violated (such as through the use of zero-padding), or when nonlinear conditions arise, numerical methods become necessary. In such situations, techniques like polynomial interpolation, used to linearize the window function over the analysis interval, combined with a subsequent NR solver, can efficiently solve problems that would otherwise be computationally difficult for real-time applications [18].

A Vandermonde matrix (VM) is a specific array where each row is a geometric progression, meaning its elements are powers of a corresponding base value, typically starting with the zeroth power. The coefficients of an arbitrary interpolating polynomial (IP) of degree $d \in \mathbb{N}$ are determined using the VM $\mathbf{V}$ [19]. In the bi-variate case [20], $\mathbf{V}$ is built by evaluating the output z_i of the auxiliary function at the points $(x_i, y_i), i \in 1, \ldots, (d+1)^2$. Assuming a polynomial

$$\mathrm{IP}(x, y) = \sum_{g=0}^{d} \sum_{h=0}^{d} c_{g,h} x^h y^g \tag{5}$$

a system of m linear equations can be formulated by evaluating the IP at m given data points (x_i, y_i), where z_i is the known function value at the coordinates $z_i = f(x_i, y_i)$, sampled in a given domain of the function being interpolated. This allows us to write the interpolation problem in its linear matrix form as

$$\mathbf{Vc} = \mathbf{z} \tag{6}$$

$$\mathbf{c} = \mathbf{V}^{-1}\mathbf{z} \tag{7}$$

with $\mathbf{c}$, being the vector containing the unknown coefficients $c_{k,l}$, $\mathbf{z}$ the output vector, and $\mathbf{V}$ the square VM of rank $(d+1)^2$

$$\mathbf{V} = \begin{bmatrix} v_1 \\ v_2 \\ \vdots \\ v_m \end{bmatrix} \tag{8}$$

with row vectors v_i

$$v_i = \left[x_i^0 y_i^0, x_i^1 y_i^0, \ldots, x_i^d y_i^0, x_i^0 y_i^1, x_i^1 y_i^1, \ldots, x_i^d y_i^d\right]. \tag{9}$$

As can be appreciated in (7), the VM procedure reduces the interpolation problem to an operation of linear algebra.

C. Bi-Variate Newton-Raphson Method

Another foundational component necessary to apply an approach analogous to [16] is a bi-variate NR. It is used to find the local root of a function, with an important impact on the analysis of functions of implicit or non-linear nature [21]. To apply the bi-variate NR recursively, we begin with an initial guess

$$\mathbf{x}^{(\mathbf{0})} = \left(x_1^{(0)}, x_2^{(0)}\right)^T \tag{10}$$

and iterate as follows:

$$\mathbf{x}^{(l)} = \mathbf{x}^{(l-1)} - \left(\mathbf{J}(\mathbf{x}^{(l-1)})\right)^{-1} \mathbf{f}(\mathbf{x}^{(l-1)}) \tag{11}$$

here, $\mathbf{J}$ represents the Jacobian Matrix, containing the first partial derivative of $\mathbf{f}(\mathbf{x})$, in the case below, represented for two variables, i.e.,

$$\mathbf{J}(\mathbf{x}) = \frac{\partial \mathbf{f}}{\partial \mathbf{x}} = \begin{bmatrix} \frac{\partial f_1}{\partial x_1} & \frac{\partial f_1}{\partial x_2} \\ \frac{\partial f_2}{\partial x_1} & \frac{\partial f_2}{\partial x_2} \end{bmatrix}. \tag{12}$$

The method converges quadratically when $\mathbf{J}$ is non-singular, and the function exhibits monotonicity and boundedness in the neighborhood of the root. More in detail, monotonicity ensures that the function changes consistently, so each iteration moves closer to the solution rather than oscillating or diverging. Boundedness confines the iterations to a region where the function and its derivatives remain stable, preventing instability due to singularities or unbounded Jacobian values. Together, these conditions provide a controlled environment that supports stable and predictable NR convergence, when the second-derivative $\mathbf{D^2f}$ is bounded around the root [22].

III. Proposed Method Formulation

In this section, we present the IpQPFT method for the ROCOF-DFT, a required procedure so that the ROCOF-DFT becomes practical for real-time applications. The Hann window is adopted following the methodology in [13], but the formulation is valid for other window functions as well, as it is based on [16]. The practical difficulty addressed in this section is not the definition of the quadratic-phase transform itself, but the bidimensional interpolation problem that arises when ROCOF is explicitly embedded in the transform kernel.

A. IpQPFT for Rocof-Dft Formulation

When the ROCOF-DFT kernel is interpreted as a quadratic-phase Fourier transform, a major distinction arises between the classical IpDFT problem and the interpolation process of a QPFT. As shown in Fig. 1, the latter imposes the interpolation of a surface instead of a line. In this work, the local "magnitude tube" denotes the restricted region of the ROCOF-DFT magnitude surface surrounding the dominant spectral mode, obtained by following the dominant frequency region along the scanned ROCOF axis. This local region constrains the NR refinement and reduces the risk of convergence toward distant spurious maxima. As a consequence of the 2-D interpolation, the maximum within the analyzed region can be hidden between four bins. To find it, we can perform the IpDFT procedure on the frequency axes of each ROCOF bin that result from (4), e.g., via the procedure in [16], or [23]. This process determines which of the ROCOF bins contains the phasor P_m of maximum magnitude. From here, we can draw analogies between the IpDFT and IpQPFT, as illustrated in Fig. 2.

In consequence, the true frequency and ROCOF values can be expressed as

$$f_0 = \left(k_m + \delta - \frac{\rho}{2 \cdot f_{\mathrm{res}}}\right) \cdot f_{\mathrm{res}} \tag{13}$$

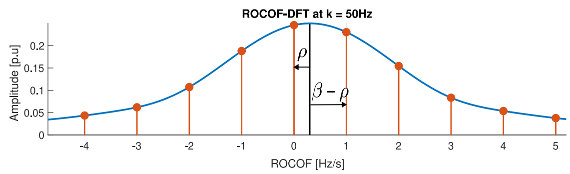

Fig. 2. Hann windowed ROCOF-DFT "transversal cut" (i.e., bidimensional plot of the ROCOF axis, fixed at the 50 Hz frequency component).

$$R_0 = (r_m + \rho) \cdot f_{\text{res}}. \tag{14}$$

Here, δ is the dimensionless fractional offset along the frequency axis, while ρ is the local ROCOF-axis offset of the spectral peak, expressed in 1/s. The quantities k_m and r_m denote the selected frequency-bin index and ROCOF-axis coordinate, respectively, and $f_{\text{res}} = F_s/N$ is the frequency-bin spacing. Thus, f_0 and R_0 are expressed in Hz and Hz/s, respectively: ρ/f_{res} is dimensionless in (13), whereas $(r_m + \rho)f_{\text{res}}$ in (14) has units of Hz/s. In this context, δ and ρ are constrained to the range

$$\delta \in [-0.5, +0.5], \quad \rho \in [-0.5, +0.5] \text{ s}^{-1}. \tag{15}$$

Moreover, the direction of the frequency displacement is defined by the ε term as

$$\varepsilon = \text{sgn}(|X[k_m + 1, r_m]| - |X[k_m - 1, r_m]|) \tag{16}$$

where its sign indicates whether the true frequency lies to the right ($\varepsilon = +1$) or to the left ($\varepsilon = -1$) of the bin k_m. Likewise, the ROCOF displacement β is given by

$$\beta = \text{sgn}(|P(r_m + 1)| - |P(r_m - 1)|) \tag{17}$$

where $|P(r_m + 1)|$ and $|P(r_m - 1)|$ denote the IpDFT-estimated phasor magnitudes of the adjacent ROCOF bins. Now, the values of the spectral magnitude at $X[k_m + \varepsilon, r_m]$, together with the spectral magnitude of $|X[k_{m_\beta}, r_m + \beta]|$, yield the IpQPFT correction equations. In the following, W denotes the 2-D response of the adopted Hann-windowed ROCOF-DFT kernel in the local frequency–ROCOF coordinates. It therefore represents the window-response term used for the interpolation, analogously to the window response in conventional IpDFT methods, but extended to the coupled frequency–ROCOF plane. The correction equations are then written as

$$\frac{|X[k_m + \varepsilon, r_m]|}{|X[k_m, r_m]|} = \frac{\left|W\left(\varepsilon - \delta - \frac{\rho}{2 \cdot f_{res}}, -\rho\right)\right|}{\left|W\left(-\delta - \frac{\rho}{2 \cdot f_{res}}, -\rho\right)\right|} \tag{18}$$

for the adapted frequency-domain tracking version, and

$$\frac{\left|X[k_{m_\beta}, r_m + \beta]\right|}{|X[k_m, r_m]|} = \frac{\left|W\left(-\delta - \frac{\rho - \beta}{2 \cdot f_{res}}, \beta - \rho\right)\right|}{\left|W\left(-\delta - \frac{\rho}{2 \cdot f_{res}}, -\rho\right)\right|} \tag{19}$$

for its ROCOF-domain tracking counterpart, being k_{m_β} the frequency bin of the maximum that gives place to $|P(r_m + \beta)|$. It can be appreciated that the frequency component is also coupled to the ROCOF component. Moreover, these relations are used as local model-based interpolation equations under the assumed single-tone quadratic-phase signal model, rather than as strict equalities for arbitrary disturbed signals.

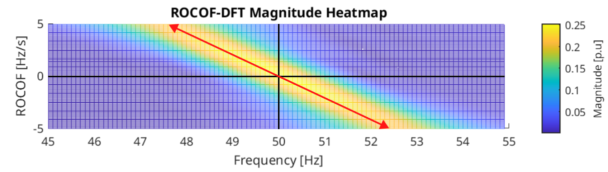

Fig. 3. ROCOF-DFT magnitude heatmap illustrating the ROCOF-induced displacement of the spectral maximum in the frequency–ROCOF plane. The arrows indicate the displacement of the maximum location in the frequency–ROCOF plane, not magnitude differences.

1) Interpolated Polynomials Construction: To construct the Multivariate Vandermonde matrices of degree $d \in [8, 10]$ (as suggested in [16]), we define two bi-variate polynomials that describe the functions necessary for the IpQPFT equations of the ROCOF-DFT, i.e., (18) and (19), by setting

$$z_{fi} = \frac{|X_i[k_m + \varepsilon, r_m]|}{|X_i[k_m, r_m]|} \tag{20}$$

for the frequency-tracking $\text{IP}_f(\delta, \rho)$, and

$$z_{Ri} = \frac{\left|X_i[k_{m_\beta}, r_m + \beta]\right|}{|X_i[k_m, r_m]|} \tag{21}$$

for the ROCOF-tracking $\text{IP}_R(\delta, \rho)$. This is achieved by extracting d + 1 ROCOF-DFT values X[k,r] of a signal

$$x[n] = A \cdot \cos\left(\phi_0 + 2\pi f_0 \frac{n}{F_s} + \pi R_0 \frac{n^2}{F_s^2}\right) \tag{22}$$

with A being the signal amplitude of value 1 p.u. The VMs can then be populated, following (9), by varying δ, and ρ in the regions defined by (15). More specifically, the interval between different frequency deviation points δ_i and ρ_i to be used for the interpolation can be defined using either simple equidistant points or Chebyshev nodes, the latter offering improved accuracy by reducing errors and the effect of Runge's phenomenon [24]. The calculated points δ_c, together with $\rho_i = \rho_c$, lead us to

$$\delta_i = \delta_c - \frac{1}{2} \cdot \frac{\rho_c}{f_{res}} \tag{23}$$

which yield the frequency and ROCOF estimates as

$$f_i = f_n + \delta_i \cdot f_{res} \tag{24}$$
$$R_i = \rho_i \cdot f_{res} \tag{25}$$

where f_n is the nominal frequency of the grid, which allows the interpolation to account for the effects of self-interference and reduces the need for explicit self-interference compensation of the fundamental tone, as in [25], or [26]. Including the ROCOF term in the frequency axis compensates the apparent frequency shift induced by nonzero ROCOF, as illustrated in Fig. 3. In the example, a signal with $f_0 = 49.5$ Hz and $R_0 = 1$ Hz/s appears close to the 50 Hz region when only the $r = 0$ slice is considered. The arrows in Fig. 3 indicate the displacement of the spectral maximum in the frequency–ROCOF plane, not amplitude differences.

Then, the values of the matrix $\mathbf{V}$ can be used in the construction of all the IPs depending on δ and ρ.

Observation: To improve interpolation accuracy, polynomial coefficients must be generated separately for each sign combination of ε and β. Additionally, the monotonicity of IP_R

depends on the sign of ε, requiring the use of the positive ROCOF term when $\varepsilon > 0$ and the negative ROCOF term when $\varepsilon < 0$ in (21).

B. Bi-Variate Newton-Raphson Solver

For real-time interpolation of the signal processed through the ROCOF-DFT, the interpolation parameters δ and ρ can be extracted by iterating (11) until convergence, using the following initial guess:

$$\mathbf{x}^{(0)} = (\delta_{P_m}, 0)^T \tag{26}$$

where δ_{P_m} is the frequency deviation obtained for the estimation of the phasor P_m. Moreover, the Jacobian can be constructed for recursive use by making

$$\mathbf{J}(\mathbf{x}) = \begin{bmatrix} \frac{\partial\,\mathrm{IP}_f}{\partial\,\delta} & \frac{\partial\,\mathrm{IP}_f}{\partial\,\rho} \\ \frac{\partial\,\mathrm{IP}_r}{\partial\,\delta} & \frac{\partial\,\mathrm{IP}_R}{\partial\,\rho} \end{bmatrix} \tag{27}$$

and, finally

$$\mathbf{f}(\mathbf{x}^{(l-1)}) = (\mathrm{IP}_f(\delta^{(l-1)}, \rho^{(l-1)}), \quad \mathrm{IP}_R(\delta^{(l-1)}, \rho^{(l-1)}))^T. \tag{28}$$

C. Parameters Estimation

The different estimated parameters $(\hat{A}, \hat{\phi}, \hat{f}, \hat{R})$ can be calculated as follows. While the initial frequency and ROCOF are calculated directly from the results of the NR process, amplitude and phase estimation require constructing the corresponding IPs and evaluating using (6).

1) Amplitude Estimation: Using the **V** matrix from Section III-A1, we construct an $\mathrm{IP_A}$, i.e., the IP for amplitude extraction by considering

$$\frac{|X[k_0, r_0]|}{|X[k_m, r_m]|} = \frac{|W[0, 0]|}{|W[-\delta, -\rho]|} \tag{29}$$

with $|X[k_0, r_0]|$ representing the estimated amplitude, and $|W[0, 0]|$ the window function at the bins [0,0]. If we assume $|X[k_0, r_0]| = \mathrm{A} = 1$ p.u. during the construction process

$$z_{Ai} = \frac{1}{|X_i[k_m, r_m]|} \tag{30}$$

and we can estimate the amplitude as

$$\hat{A} = |X[k_m, r_m]| \cdot \mathrm{IP}_A(\delta, \rho). \tag{31}$$

2) Phase Estimation: To the extent of our knowledge, there exists no analytical model describing the phase behavior of the window function along the newly introduced axis. Nonetheless, we can resort to a method analogous to the amplitude parameter extraction, by using **V**. In particular, we consider

$$\arg\left(\frac{X[k_0, r_0]}{X[k_m, r_m]}\right) = \arg\left(\frac{W[0, 0]}{W[-\delta, -\rho]}\right) \tag{32}$$

which leads to

$$\begin{aligned} &\arg(X[k_0, r_0]) - \arg(X[k_m, r_m]) \\ &\quad = \arg(W[0, 0]) - \arg(W[-\delta, -\rho]). \end{aligned} \tag{33}$$

Given that the estimated phase angle is $\hat{\phi}_0 = \arg(X[k_0, r_0])$ and, by definition, $\arg(W[0, 0]) = 0$, we obtain

$$\hat{\phi}_0 = \arg(X[k_m, r_m]) - \arg(W[-\delta, -\rho]). \tag{34}$$

In consequence, the phase estimation IP_ϕ is given by

$$z_{\phi i} = -\arg(W[-\delta_i, -\rho_i]) \tag{35}$$

assuming $\phi_0 = 0$. Thus, the phase estimate becomes

$$\hat{\phi}_0 = \arg(X[k_m, r_m]) - IP\phi(\delta, \rho). \tag{36}$$

A polynomial degree of 2 is recommended. Furthermore, to obtain a phase aligned with the PMU standard, the result must be shifted to the midpoint of the window, according to (3), since ϕ_0 represents the phase at the beginning of the processed window. Hence,

$$\hat{\phi} = \hat{\phi}_0 + \hat{f}_0 \cdot t_{mid} + \frac{1}{2}\hat{R} \cdot t_{mid}^2 \tag{37}$$

where t_{mid} is half the observation window period

$$t_{mid} = \frac{1}{2 \cdot f_{res}}. \tag{38}$$

3) Frequency Estimation: The frequency parameter is defined by (13). Because the PMU standard requires frequency to be referenced to the midpoint of the observation window, we substitute t_{mid} into (2), using the result from (14) as ROCOF parameter.

4) Rocof Estimation: On the other hand, for ROCOF reporting at high reporting rates, i.e., $F_{rep} > 20$ frames per second (fps), the ROCOF measurand is more appropriately obtained as the backward-Euler derivative of the reported frequency, since it is inherently referenced to the reporting interval and therefore provides a more local representation of the frequency slope. In contrast, the ROCOF estimated by the IpQPFT [(14)] is a model-based parameter identified over the full observation window, namely, the constant-ROCOF term that best reproduces the phase evolution within that interval. Accordingly, under rapidly varying conditions, the IpQPFT-based ROCOF should be interpreted as the equivalent constant-ROCOF parameter associated with the observation window, rather than as a strictly local measurand, since higher-order in-window phase variations are effectively absorbed into the fit parameter, as demonstrated in Section IV-B. For this reason, the IpQPFT ROCOF is more appropriately interpreted as an internal model-based estimate, while the backward-Euler formulation is better suited for ROCOF reporting at high reporting rates. At lower reporting rates, i.e., $F_{rep} \leq 20$ fps, the IpQPFT estimate remains more advantageous, as the identification of a constant-ROCOF term over the observation window can provide a closer representation of the dominant underlying trend. Since this work emphasizes a reporting rate of 50 fps, the reported ROCOF is restricted to the backward-Euler formulation

$$\hat{R}_{\mathrm{BE}}[l] = \left(\hat{f}[l] - \hat{f}[l-1]\right) F_{\mathrm{rep}} \tag{39}$$

where $\hat{f}[l]$ is the reported frequency at frame l, and F_{rep} is the reporting rate. To improve robustness during strong dynamic conditions, the resulting ROCOF is conditionally smoothed by a causal second-order Butterworth low-pass IIR filter with cutoff frequency $f_c = 6$ Hz. The filter is activated only when the variation of the model-based ROCOF estimate exceeds a threshold, namely, $|\hat{R}[l]-\hat{R}[l-1]| > R_{\text{th}}$, with $R_{\text{th}} = 1$ Hz/s, and remains active for a finite hold time T_{hold} to account for the transient contamination of consecutive observation windows after the disturbance. Accordingly, the reported ROCOF is given by $\hat{R}_{\text{rep}}[l] = \text{IIR}_{\text{LP}}\{\hat{R}_{\text{BE}}[l]\}$ during the hold interval, and by $\hat{R}_{\text{BE}}[l]$ otherwise, providing a causal tradeoff between noise rejection and reporting responsiveness.

D. Rocof-Dft Candidate Selection and COI-Based Parameter Fusion

Under fault or strong dynamic conditions, the magnitude surface of the ROCOF-DFT may exhibit multiple local maxima along the ROCOF axis within the same observation window. In such cases, selecting the dominant candidate solely by magnitude may lead to abrupt mode switching, since the strongest local maximum is not always the one most consistent with the recent signal evolution. To mitigate this effect, the current IpQPFT implementation incorporates two complementary robustness measures under multiple-maxima conditions: continuity-aware candidate selection and center-of-inertia (COI) fusion. The first biases the candidate selection toward solutions compatible with the previous valid estimate, whereas the second avoids hard switching when multiple ROCOF modes are detected. From a methodological viewpoint, the continuity-aware score is not intended as an exact posterior density, but as a posterior-like additive criterion based on MAP formulations, where likelihood and regularization contributions naturally appear in logarithmic form [27].

Accordingly, each ROCOF-axis candidate is scored not only by its magnitude, but also by continuity penalties associated with deviations from the previously estimated frequency and ROCOF. Let $(\hat{f}_i, \hat{R}_i, \hat{A}_i)$ denote the frequency, ROCOF, and magnitude associated with the ith candidate, let ε denote a small positive regularization constant introduced to avoid numerical singularities in the logarithmic term, and let σ_f^{sel}, which controls how strongly a candidate is penalized for deviating from the previous frequency; σ_R^{sel}, controlling how strongly a candidate is penalized for deviating from the previous ROCOF; and σ_{R0}^{sel}, in charge of the weak pull toward zero ROCOF. All three denote positive tuning parameters controlling the frequency-continuity, ROCOF-continuity, and ROCOF regularization penalties, respectively, with smaller σ implying stronger penalty, and more continuity enforcing, while larger values favor changes and transition. The continuity-aware score is defined as

$$\Lambda_i^{\text{cand}} = \log(\hat{A}_i^2 + \varepsilon) - \Delta f_i^{\text{cand}} - \Delta R_i^{\text{cand}} \tag{40}$$

where

$$\Delta f_i^{\text{cand}} = \frac{1}{2}\left(\frac{\hat{f}_i - \hat{f}_{k-1}}{\sigma_f^{\text{sel}}}\right)^2 \tag{41}$$

and

$$\Delta R_i^{\text{cand}} = \frac{1}{2}\left(\frac{\hat{R}_i - \hat{R}_{k-1}}{\sigma_R^{\text{sel}}}\right)^2 + \frac{1}{2}\left(\frac{\hat{R}_i}{\sigma_{R0}^{\text{sel}}}\right)^2 \tag{42}$$

with:

1) $\sigma_f^{sel} = 0.75 \cdot f_{res}$, i.e., 0.75 frequency bins;
2) $\sigma_R^{sel} = f_{res}$, i.e., one ROCOF bin;
3) $\sigma_{R0}^{sel} = 4 \cdot f_{res}$, i.e., weak pull-to-zero.

The center candidate is then selected as the maximizer of Λ_i^{cand}. The logarithmic amplitude term introduces the candidate magnitude as a proxy for relative evidence while preserving an additive score structure; after exponentiation and normalization, this yields weights proportional to amplitude evidence rather than to an excessively sharp exponential of amplitude. In this way, preference for high-energy candidates is preserved, while physically inconsistent jumps in frequency and ROCOF are penalized.

When multiple relevant ROCOF modes are detected, the estimator does not enforce a hard decision. Instead, the refined modes are combined through a COI strategy. For each mode m, a posterior-like score is defined in the same form as

$$\Lambda_m = \log(\hat{A}_m^2 + \varepsilon) - \Delta f_m - \Delta R_m \tag{43}$$

where σ_f, σ_R, and σ_{R0} are positive tuning parameters that play the same role at the fusion stage, with more permissive σ-parameter values, so two modes can still be blended instead of one being overly-suppressed. Accordingly

$$\Delta f_m = \frac{1}{2}\left(\frac{\hat{f}_m - \hat{f}_{k-1}}{\sigma_f}\right)^2 \tag{44}$$

and

$$\Delta R_m = \frac{1}{2}\left(\frac{\hat{R}_m - \hat{R}_{k-1}}{\sigma_R}\right)^2 + \frac{1}{2}\left(\frac{\hat{R}_m}{\sigma_{R0}}\right)^2 \tag{45}$$

with $\sigma_f = f_{res}$, $\sigma_R = 2 \cdot f_{res}$, and $\sigma_{R0} = 5 \cdot f_{res}$. Moreover, the COI-fusion weight is calculated as

$$w_m = \frac{\exp(\Lambda_m)}{\sum_\ell \exp(\Lambda_\ell)}. \tag{46}$$

The reported magnitude, frequency, and ROCOF are subsequently obtained by weighted averaging

$$\hat{A}_k = \sum_m w_m \hat{A}_m, \quad \hat{f}_k = \sum_m w_m \hat{f}_m, \ \hat{R}_k = \sum_m w_m \hat{R}_m \tag{47}$$

while phase is combined through a circular weighted mean, with ϕ_{ref} denoting the previous valid phase estimate. The fused phase is then obtained as

$$\hat{\phi}_k = \phi_{\text{ref}} + \angle\left(\sum_m w_m e^{j(\hat{\phi}_m - \phi_{\text{ref}})}\right). \tag{48}$$

Therefore, the IpQPFT estimator still relies on the original quadratic-phase model, while gaining robustness against transient multi-peak ambiguity and unstable mode switching.

IV. Tests and Results

Hereafter, we present the results of the methods proposed in Section III. If not specified otherwise, the default values for the peak amplitude, initial phase position, and frequency of the signals discussed in the current article are defined as follows.

1) *RMS Amplitude:* $|\mathrm{X_m}| = 1$ p.u.
2) *Signal Phase Angle:* $\angle\mathrm{X} = 0$ rad.
3) *Fundamental Frequency:* $\mathrm{f_0} = 50$ Hz.

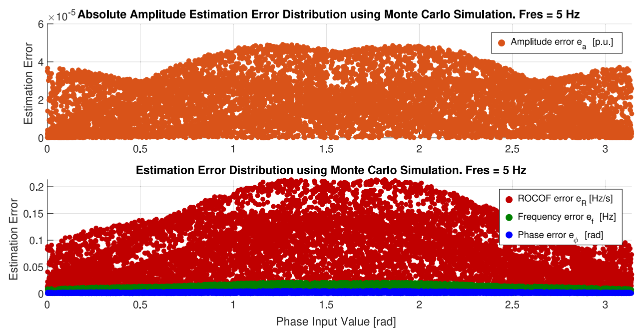

Fig. 4. Absolute error distributions of amplitude, ROCOF, frequency, and phase for a 10-cycle observation window, as obtained in a Monte Carlo simulation with 10 000 iterations.

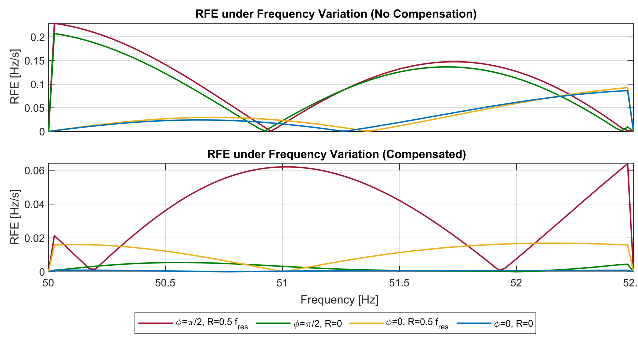

Fig. 5. Absolute RFE under frequency variation, with fixed phase and ROCOF conditions.

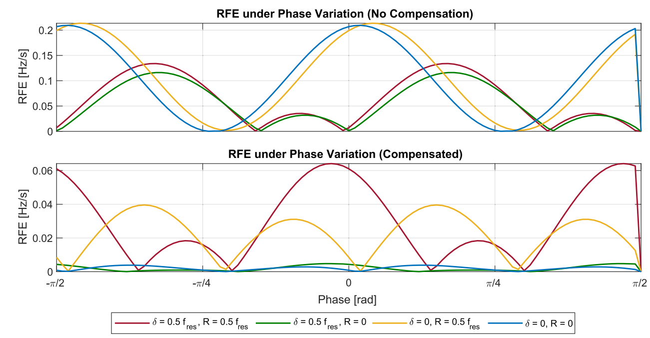

Fig. 6. Absolute RFE under phase variation, with fixed frequency and ROCOF conditions.

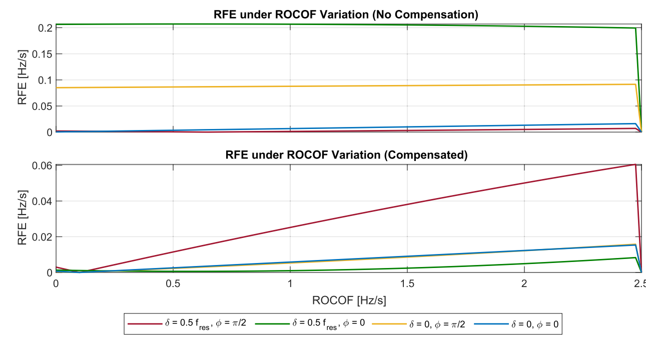

Fig. 7. Absolute RFE under ROCOF variation, with fixed phase and frequency conditions.

Also, the following algorithmic parameters will be assumed, if not stated otherwise.

1) *Observation Window:* 10 cycles, i.e., $f_{res} = 5$ Hz.
2) *Sampling Frequency:* $F_s = 10$ kHz.
3) *PMU Reporting Rate:* $F_{rep} = 50$ Hz.

A. Error Characterization and Compensation

Analyzing the error behavior of an estimation algorithm is key for understanding its limitations and identifying possible space for further performance improvements, such as systematic error compensation.

In general, the parameters of the test signals cover the following ranges.

1) $\phi \in [-(\pi/2), (\pi/2)]$ rad.
2) $\delta \in [0, 0.5 f_{res}]$ Hz.
3) $R \in [0, 0.5 f_{res}]$ Hz/s.

The characterization method used in Fig. 4 is the Monte Carlo simulation, showing that the ROCOF parameter estimation experiences the highest absolute error of the examined parameters, with a value of around 0.22 Hz/s. In comparison, the absolute phase and frequency errors were less pronounced, consistent with other IpDFT methods, keeping in the range of a few units of mrad and mHz, respectively. The amplitude error is even lower in magnitude, staying on the order of 10^{-4} p.u. Accordingly, the investigation focuses primarily on the ROCOF error (RFE), evaluating the extent to which off-nominal parameter variations influence this metric.

Next, Figs. 5–7 present the outcome of individually-varying parameters, while the other two remain static. The upper subplots represent stages without compensation, and the lower ones after compensation. From Figs. 5 and 6, it can be clearly observed that varying individually frequency or phase parameters produces a sinusoidal RFE trajectory (also observed in frequency and phase), revealing a systematic dependence on both parameters, with a maximal value found at the vicinity of 0.22 Hz/s, which stays in accordance to the Monte Carlo simulations. The respective sinusoidal trajectories take 2 different trends depending on the offset magnitude of the fixed frequency or phase value. Nonetheless, from Fig. 7, we can infer that the ROCOF value has little influence on the RFE. This is confirmed by Fig. 7, where a variation in the ROCOF resulted in almost constant RFE. This insight into the bivariate dependency of the RFE was helpful in devising a compensation procedure for the respective trends.

To compute the compensation value, we use a polynomial interpolation method, as explained in Section III, analogous to the amplitude and phase estimation. In this case, the VM is formed from the reported errors evaluated at selected frequency–phase pairs in the aforementioned ranges. Given that the estimation process is effectively insensitive to ROCOF variations (as evidenced in Fig. 7), this parameter can be excluded from the compensation process. More in detail, the compensation values (ϕ_0, δ), resulting from the parameters extraction, determine the compensation values for our bivariate compensation polynomials IP_c, allowing us to update the estimate. The same procedure can be applied to compensate for frequency and phase errors.

The compensated RFEs show four times better accuracy, as the maximum value decreased to around 0.06 Hz/s. After compensation, the RFE trajectories in frequency and phase variation maintained the sinusoidal nature and a linear dependency on the ROCOF values.

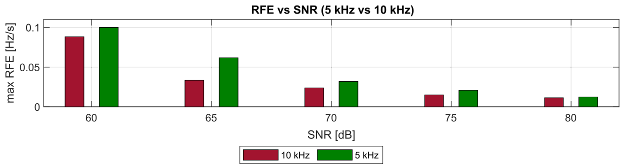

Fig. 8. Maximum RFE in dependency of the SNR with 10 kHz and 5 kHz sampling frequencies.

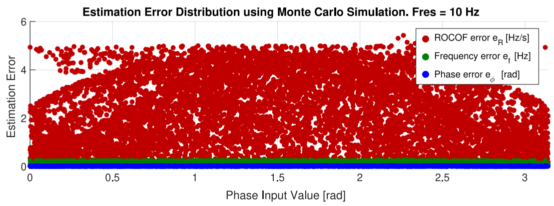

Fig. 9. Absolute error distribution of ROCOF, frequency, and phase estimation for a 5-cycle observation window, placed together, as obtained in a Monte Carlo simulation with 10 000 iterations.

Finally, estimation performance after compensation is further examined under different signal-to-noise ratios (SNRs) and varying sampling frequencies. The results presented in Fig. 8 show that satisfying performance is reached when the SNR is higher than 65 dB. In this case, $F_s = 10$ kHz is necessary. For better SNR conditions, the noise impact on the estimation for $F_s = 5$ kHz, and $F_s = 10$ kHz shows no significant improvement.

B. CRLB Interpretation of FE and RFE

In this section, the results are discussed under the light of the Cramer–Rao lower bound (CRLB), which complements the discussion on the FE variability increase observed when reducing the observation window from $T = 0.2$ s (10 cycles) to $T = 0.1$ s (5 cycles), as presented in Fig. 9. In both scenarios, the post-compensation FE standard deviation is empirically found to increase by approximately one order of magnitude

$$\frac{\sigma_{\mathrm{FE}}(0.1)}{\sigma_{\mathrm{FE}}(0.2)} \approx 10. \tag{49}$$

The key interpretation is that, relative to quasi-stationary DFT-based estimators, explicitly introducing ROCOF as a state variable shifts a significant portion of the uncertainty from the frequency domain into the ROCOF domain, as this is the highest-order modeled parameter. Under the constant-ROCOF model adopted by the IpQPFT formulation, the signal phase is quadratic (i.e., $dR/dt = 0$), and the instantaneous frequency follows (2). Considering the analytic signal observed in AWGN with independent samples, and defining $\mathrm{SNR} = A^2/\sigma^2$. In consequence, the Fisher information matrix (FIM) associated with estimating (f_0, R) is governed by the phase sensitivities

$$\partial\phi/\partial f_0 \propto n, \quad \text{and } \partial\phi/\partial R \propto n^2. \tag{50}$$

When the parameterization is referenced to the midpoint of the observation window, the FIM is approximately diagonal, leading to the following CRLBs for unbiased estimation:

$$\mathrm{Var}(f_0) \geq \frac{3F_s^2}{2\pi^2 N(N^2-1)\mathrm{SNR}} \tag{51}$$

and

$$\mathrm{Var}(R) \geq \frac{120F_s^4}{\pi^2 N(3N^4-10N^2+7)\mathrm{SNR}} \tag{52}$$

where N is the number of samples in the observation window.

Two points follow directly from (51), and (52).

1) *Improvement Cost for Reduced Frequency Variance:* Introducing R as an additional estimated parameter does not lower the noise-limited bound on $\mathrm{Var}(f_0)$ relative to a frequency-only (quasi-stationary) model. In other words, the best-achievable f_0 variance remains fundamentally constrained by the same scaling with N and SNR.
2) *RFE Absorbs Phase Curvature and Model Mismatch:* The additional degree of freedom R carries a bound that decays more slowly with shorter windows (for large N, $\mathrm{Var}(f_0) \propto N^{-3}$ whereas $\mathrm{Var}(R) \propto N^{-5}$). Consequently, any phase dynamics not representable by the quadratic model (e.g., higher-order dynamics or abrupt changes within the window) is injected in the highest-order available term, i.e., in the ROCOF estimate.

This explains the practical variability shift often observed when comparing against common DFT-based estimators: in a quasi-stationary IpDFT setting, ROCOF is implicitly constrained to $R = 0$ and is typically obtained a posteriori by finite differences of successive frequency estimates. Under a nonzero ROCOF, the model becomes intrinsically biased, and the resulting mismatch manifests primarily as frequency/phase error. In contrast, explicitly estimating R restores model consistency with the phase-based ROCOF definition, and the dominant uncertainty under dynamic conditions appears primarily in the estimated ROCOF, while the estimated frequency remains largely unbiased.

1) Propagation to FE at the PMU Reporting Instant: In the proposed formulation, the PMU standard requires frequency to be referenced to the midpoint of the observation window. Thus, the frequency variability after ROCOF-based compensation is lower-bounded by the joint uncertainty of the estimated (f_0, R), and can be decomposed as

$$\mathrm{Var}(f_{\mathrm{mid}}) \approx \mathrm{Var}(f_0) + t_{\mathrm{mid}}^2\mathrm{Var}(R) + 2t_{\mathrm{mid}}\mathrm{Cov}(f_0, R) + \mathrm{Var}_{\mathrm{alg}} \tag{53}$$

where $\mathrm{Var}_{\mathrm{alg}}$ groups implementation effects beyond the noise-limited bound.

If the estimator is efficient (i.e., near-CRLB), and the covariance is small due to midpoint referencing, then using (51), and (52), implies $\mathrm{Var}(f_{\mathrm{mid}}) \propto T^{-3}$, hence halving the window from 0.2 s to 0.1 s yields an expected increase of σ_{FE} of about $2^{3/2} \approx 2.83$, which, according to Fig. 9, is enough to make the estimator fail the PMU standard FE requirements (i.e., 5 mHz), achieving up to 10 times lower FE after compensation (i.e., reducing the FE from ≈200 mHz to ≈20 mHz, shown in Section IV-E). Therefore, the measured value of ≈10 times increase in (49) indicates that, at $T = 0.1$ s, the dominant term is $\mathrm{Var}_{\mathrm{alg}}$ rather than the CRLB-only contribution.

2) Estimator Efficiency Limitation for Lower Observation Windows: In the IpQPFT implementation, (δ, ρ) are recovered by solving the two correction equations via the interpolated polynomials $\mathrm{IP}_f(\delta, \rho)$ and $\mathrm{IP}_R(\delta, \rho)$ and a bi-variate NR iteration. The NR update requires the inversion (or equivalent solution) of the Jacobian (27). For short windows, two effects affect $\mathrm{Var}_{\mathrm{alg}}$ in (53).

1) *Poor Conditioning Along the ROCOF Dimension:* The same phase-sensitivity structure that yields $\mathrm{Var}(R) \propto T^{-5}$ also implies that, at $T = 0.1$ s, the objective surface is comparatively flat in ρ. Under this condition, small perturbations in the local polynomial model (e.g., noise, discretization, or interpolation residuals) are amplified by the NR step through the Jacobian inversion, inflating the estimated ROCOF beyond the noise-limited CRLB.
2) *Coarse 2-D Sampling and Increased Relative Approximation Error:* Reducing the observation period increases the bin spacing in both axes, so the peak neighborhood is sampled more sparsely. The resulting increase in relative local-model error in IP_f and IP_R makes the refinement more sensitive to the initial guess and convergence conditions, which directly increases the observed variability.

These effects explain why the empirical increase in FE can exceed the CRLB-driven factor of 2.83 times and reach $\approx$10 times at $T = 0.1$ s: this implies the estimator departs from the efficient regime and becomes dominated by implementation-dependent uncertainty.

C. Overview of the Compressive Sensing Taylor-Fourier Multifrequency Algorithm

As part of the comparative analysis, we introduce the CSTFM phasor-estimation algorithm, characterized by its good performance in the dynamic parameters estimation. The CSTFM estimator builds on a generalized TFT model capable of representing multi-tone signals with arbitrary (and not necessarily harmonic) frequency content [28]. Because of this broader modeling capability, the estimator's accuracy depends strongly on the specific components included in the TFM expansion. In its original formulation, a compressive-sensing routine identifies the most significant spectral components with a resolution better than 0.5 Hz; however, this approach entails considerable computational effort.

To mitigate this issue, [17] introduced a more efficient formulation in which an orthogonal matching pursuit algorithm estimates the fundamental frequency with a resolution of 0.4 Hz. Furthermore, when the observation window satisfies $C \geq 4$ cycles, the method improves the TFM model with the four most relevant sinusoidal tones, thereby improving overall estimation accuracy. With a five-cycle window, this implementation meets both P- and M-class requirements [17].

D. Overview of TLS-ESPRIT Technique

For further comparison, we also consider the improved TLS-ESPRIT parametric method [12], proposed for dynamic synchrophasor estimation in M-class PMUs. The method models the input waveform as a sum of complex exponential modes, while representing the fundamental component through a second-order Taylor expansion so as to explicitly capture amplitude and phase variations within the observation window. To identify the signal content, the sampled data are arranged in a Hankel matrix and processed through an ESPRIT-based subspace estimation. An initial model order is first obtained from a downsampled data window, and the associated frequency estimates are then used to distinguish passband components, which are absorbed into the dynamic fundamental behavior, from stopband interferers, which are treated as separate modes. A final estimation is subsequently carried out on the full data window, after which the fundamental phasor, frequency, and ROCOF are recovered from a Taylor-extended least-squares formulation. In contrast to approaches that derive ROCOF from finite differences between consecutive frequency estimates, TLS-ESPRIT estimates it directly from the second-order phase term within a single window, which improves smoothness and robustness under dynamic conditions.

From a computational standpoint, TLS-ESPRIT is significantly more demanding than DFT-based approaches. For lower report rates ($\leq$4 fps), it is in the same class as other model-based high-resolution estimators such as CSTFM.

E. Performance Evaluation Under the IEC/IEEE 60255-118-1:2018

The PMU standard defines a set of test conditions that apply exclusively to the fundamental frequency, reproducing real-world conditions. These tests are as follows.

1) *Static Amplitude (SA) and Frequency (SF):* The rms magnitude of the fundamental component is adjusted from 0.8 p.u. to 1.2 p.u. in steps of 0.1 p.u.. The signal frequency is varied within $\pm$5 Hz using increments of 0.1 Hz.
2) *Harmonic Distortion (HD):* Individual harmonic components from the 2^{nd} to the 50^{th} order are injected, each with an rms magnitude of 1 % or 10 % of the fundamental.
3) *Dynamic Modulation:*
   a) *Amplitude (AM):* Sinusoidal modulation of 10 % amplitude at 2 Hz, and 5 Hz.
   b) *Phase (PM):* Sinusoidal modulation of 0.1 rad at 2 Hz, and 5 Hz.
4) *Frequency Ramp (FR):* The signal frequency is changed linearly until it reaches $\pm$2 Hz of distance away from the nominal value, at a rate of $\pm$1 Hz/s.

As can be appreciated in Table I, the standard-oriented assessment of the proposed IpQPFT on ROCOF-DFT reveals a configuration-dependent behavior rather than a single universally optimal PMU solution. In particular, the 10-cycle configuration satisfies the Class M and Class P requirements for the SA, SF, HD, and FR tests, thus preserving the favorable behavior of conventional IpDFT-based PMU estimators under static and quasi-static conditions while extending the signal model to explicitly account for nonzero ROCOF. In general, the method retains IpDFT-like accuracy in amplitude, phase, and frequency estimation, while improving the consistency of the estimated frequency under dynamic ramps by embedding ROCOF directly into the transform model. These results indicate that explicitly incorporating ROCOF into the DFT kernel does not penalize the estimator under the standard static and quasi-static tests with respect to ordinary IpDFT-type approaches. Under HD, the proposed method also remains compatible with the leakage-mitigation mechanisms

TABLE I

MAXIMUM ERRORS REPORTED FOR THE TESTS CONDUCTED IN ACCORDANCE WITH THE IEC/IEEE 60 255-118-1:2018 STANDARD. THE SNR LEVEL ADOPTED IS 60 dB, AS REQUIRED BY THE STANDARD

IpQPFT on ROCOF-DFT (10 Cycles)				
Carried Test	**TVE [%]**	**FE [mHz]**	**RFE [Hz/s]**	**Compliance**
SA	0.003	0.00	0.007	ClassM/P
SF	0.055	0.00	0.013	ClassM/P
1 % HD	0.004	0.07	0.009	ClassM/P
10% HD	0.033	0.06	0.079	ClassM/P
AM (k_x= 2 Hz)	1.756	41.40	0.866	ClassM/P
AM* (k_x= 2.4 Hz)	2.515	50.5	0.683	ClassM
AM* (k_x= 5 Hz)	5.483	167.40	3.212	—
PM (k_a= 2 Hz)	0.295	12.80	0.347	ClassM/P
PM* (k_a= 4 Hz)	1.946	99.80	6.553	ClassM
PM* (k_a= 5 Hz)	3.005	177.2	7.048	—
FR	0.002	0.00	0.004	ClassM/P
IpQPFT on ROCOF-DFT (5 Cycles)				
Carried Test	**TVE [%]**	**FE [mHz]**	**RFE [Hz/s]**	**Compliance**
SA	0.709	5.10	0.209	—
SF	0.705	16.10	0.675	—
1 % HD	0.711	4.70	0.206	ClassM/P
10 % HD	0.707	4.90	0.203	ClassM/P
AM (k_x= 2 Hz)	0.825	33.80	2.133	ClassM/P
AM* (k_x= 5 Hz)	1.695	124.10	2.138	ClassM
PM (k_a= 2 Hz)	0.484	5.20	1.455	ClassM/P
PM* (k_a= 5 Hz)	0.922	49.50	4.918	ClassM
FR	0.104	1.40	0.034	ClassM/P

***Only required for Class M PMU. F_{rep} defined by the standard**

commonly used in the IpDFT family, benefiting from the additional ROCOF-aware refinement stage.

The behavior under AM and PM tests is better interpreted as a window-length tradeoff. The 10-cycle realization offers the best static and quasi-static accuracy, but its larger observation window attenuates faster modulation components and therefore degrades performance as the modulation frequency increases. By contrast, shortening the window to 5 cycles improves the estimator's responsiveness to AM and PM variations, restoring compliance for the higher-rate modulation cases reported in Table I, although at the cost of increased static variability, as discussed in Section IV-B.

Overall, these results should be interpreted as a configuration-dependent characterization of the estimator rather than as evidence of uniform compliance under all operating settings. For the 10-cycle configuration, the proposed IpQPFT preserves the favorable static and quasi-static behavior typically associated with conventional IpDFT estimators, while providing improved robustness under genuine dynamic ramps, since ROCOF is explicitly incorporated into the signal model rather than treated as an external perturbation. Its advantage is not a change in the underlying DFT-interpolation philosophy, but the extension of that philosophy beyond the quasi-stationary assumption.

When compared to the CSTFM in [17], for tests where both methods are compliant, similar performance is observed. Nonetheless, the use of i-IpDFT in the peak-finding stage improves the ROCOF results for HD tests relative to CSTFM, highlighting the compatibility of the proposed approach with existing IpDFT-based techniques. Moreover, the IpQPFT delivers significantly improved performance during the FR test, as it explicitly models ROCOF as part of the estimation process, in contrast to tracking-oriented approaches that infer ROCOF indirectly.

On the other hand, when compared with [12], the TLS-ESPRIT method provides highly accurate estimates due to its parametric subspace-based formulation. However, this accuracy is achieved at the expense of a substantially higher computational cost, since the method requires Hankel-matrix construction, model-order selection, subspace decomposition, and Taylor-extended least-squares estimation. By contrast, the proposed IpQPFT remains closer to DFT-based methods, as its dominant operation is the local ROCOF-DFT evaluation followed by bounded interpolation, NR refinement, and subsequent compensation steps.

F. Comparative Analysis: 2015 Turkey Power Outage

The comparative performance analysis of the ROCOF-DFT and CSTFM estimators utilizes data from the major power outage that occurred in Turkey on March 31, 2015 [29].

The contingency was initiated by the trip of an overloaded transmission line, which divided the Turkish grid into two subsystems. This separation caused a 21 % power deficit in the western region, leading to a loss of synchronism with the Central European system.

Moreover, Frequency and ROCOF parameters were reconstructed from the acquired voltage waveforms at the Ataturk and Temelli substations using the approach detailed in [30].

The system operated stably during the pre-contingency interval. The sequence of events defining the contingency were follows.

1) *t = 4 s:* A sharp voltage decrease occurred, followed by irregular frequency fluctuations.
2) *t = 5 s:* The three interconnection lines with the Bulgarian and Greek power grids tripped.

This critical event caused the frequency to rapidly decay to 49.6 Hz, with the average ROCOF reaching −3 Hz/s. The estimated voltage waveform, phase, frequency, and ROCOF for both substations, spanning the time intervals before and after the contingency, are presented in Fig. 10 for the Ataturk substation, with an emphasis on frequency and ROCOF parameters during the fault in Fig. 11. In Fig. 12, the parameter estimation for the Temelli substation is presented, with frequency and ROCOF parameters emphasized in Fig. 13.

All methods, the IpQPFT, CSTFM, and TLS-ESPRIT, show accurate tracking of the event, with smoother performance of the IpQPFT under stable conditions. As observed in the phase and frequency reports, as these depend on the reported ROCOF, the estimated ROCOF correctly tracks the dynamic behavior of the system as shown in (37), and described in Section III-C3. So, the IpQPFT-estimated ROCOF represents the dynamic ROCOF value of the signal. Nonetheless, although the IpQPFT ROCOF estimate is directly aligned with the PMU standard definition of ROCOF as the second derivative of the signal phase with respect to time, it constitutes a window-consistent realization of this quantity. Specifically, the IpQPFT ROCOF corresponds to the constant ROCOF parameter that best fits the phase evolution over the entire

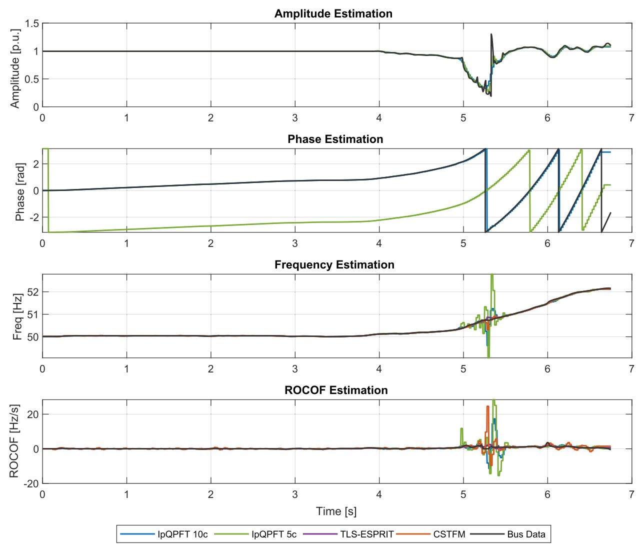

Fig. 10. Parameter estimation in the bus of Ataturk substation, Turkey, during the 31.05.2015 power-outage event.

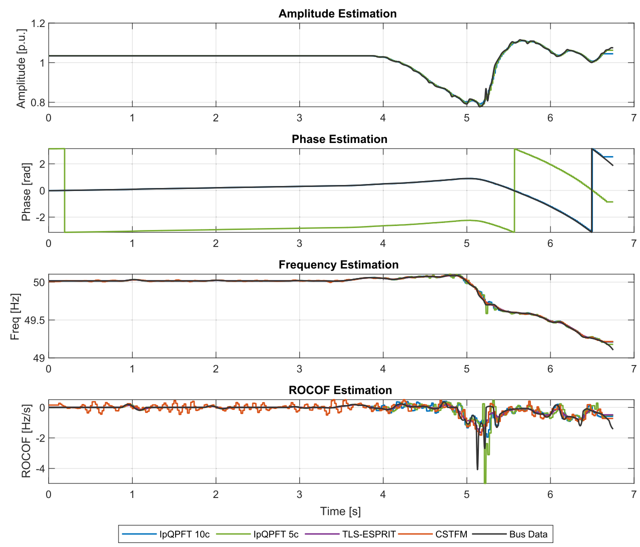

Fig. 12. Parameter estimation in Temelli bus, Turkey, during the 31.05.2015 power-outage event.

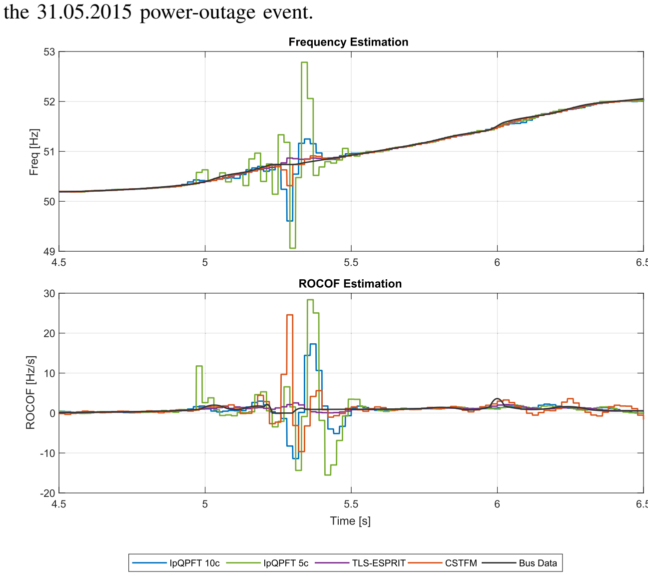

Fig. 11. Frequency and ROCOF parameter estimation focused on the event interval at the Atatürk substation bus.

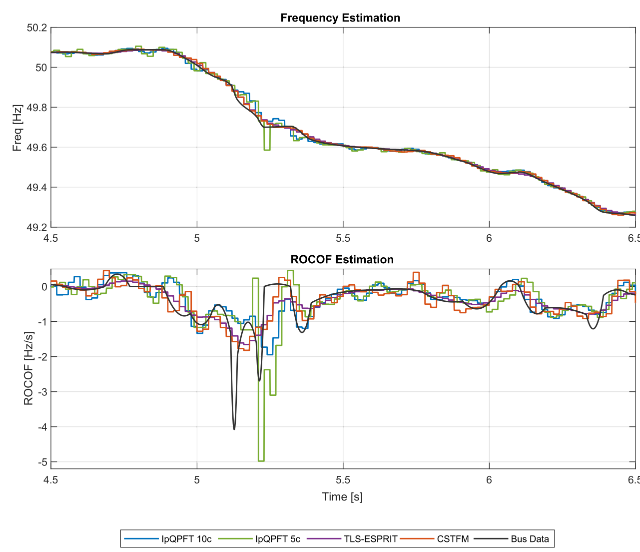

Fig. 13. Frequency and ROCOF parameter estimation focused on the event interval at the Temelli substation bus.

observation window. In contrast, ROCOF obtained by finite differencing of consecutive frequency reports represents a discrete-time approximation of the derivative of the reported frequency trajectory and is therefore aligned with the reporting interval rather than the signal observation window. During fast dynamics or regime transitions, these approaches target different measurands and are not expected to coincide. In such conditions, deviations from the constant-ROCOF assumption, such as unmodeled higher-order phase dynamics occurring within the window, are inherently projected into the ROCOF parameter, as demonstrated in Section IV-B.

G. Algorithmic Workflow and Computational Cost

The overall processing flow of the proposed algorithm is illustrated in Fig. 14, while its computational cost is summarized in Table II. The analysis is expressed in terms of dominant complex multiplication operations for the transform-evaluation stages, whereas bounded post-processing stages are represented through equivalent arithmetic-cost expressions. Minor auxiliary operations are neglected. In particular, the current implementation avoids evaluating the full ROCOF-DFT matrix: after a coarse scan at $r = 0$ identifies the dominant frequency bin k_m, the IpQPFT refinement only requires the peak bin and its immediate neighbors, i.e., the

TABLE II

SUMMARY OF THE COMPUTATIONAL COST OF THE PROPOSED IpQPFT-BASED ROCOF-DFT ESTIMATOR

Step	Operation	Cost
Ref.	Full ROCOF-DFT evaluation	$C_{\text{full}} = KRN$
3	Coarse scan at $r = 0$	$C_{f,0} = KN$
4	Local ROCOF tube evaluation	$C_{\text{tube}} = 3RN$
3–4	Optimized transform evaluation	$C_{\text{opt}} = (K + 3R)N$
6	Single-mode NR refinement	$C_{\text{NR}} = I_{\text{NR}}[3(M_f + M_R) + c_J]$
7a	COI fusion (multipeak case)	$C_{\text{COI}} = 2C_{\text{NR}} + c_{\text{fuse}}$
8	Bias compensation	$C_{\text{comp}} = 3(M_\phi^{\text{c}} + M_f^{\text{c}} + M_R^{\text{c}})$
–	Total cost, single-mode case	$C_{\text{tot}} = C_{\text{opt}} + C_{\text{NR}} + C_{\text{comp}}$
–	Total cost, multipeak case	$C_{\text{tot,COI}} = C_{\text{opt}} + C_{\text{COI}} + C_{\text{comp}}$

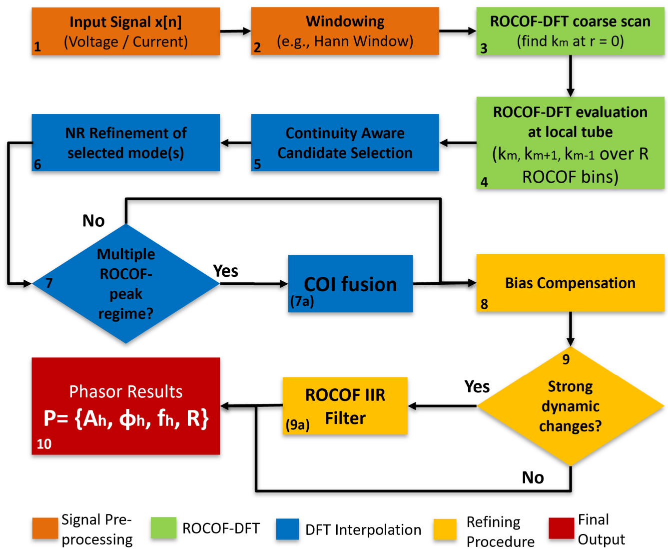

Fig. 14. Simplified flow of the proposed IpQPFT-based estimator. The open-source MATLAB code can be found in [31].

TABLE III
INPUT AND EXECUTION CONDITIONS USED IN THE COMPUTATIONAL TIMING ASSESSMENT OF THE DIFFERENT ALGORITHMS BENCHMARKING

Quantity	Value
Sampling frequency, f_s	10 kHz
Observation window, T	0.2 s
Samples per window, $N = f_s T$	2000
Reporting rate, F_{rep}	50 fps
Reporting period, T_{rep}	20 ms
Number of executions	981

local tube $k \in \{k_m - 1, k_m, k_m + 1\}$ over the complete ROCOF axis, as can be appreciated in Fig. 3, so that the transform cost is reduced to the expression presented in step 4. In the presence of a secondary frequency peak, the i-IpDFT leakage correction [6] is also performed only locally. More specifically, the support rows associated with the interferer are computed only at a limited set of relevant ROCOF-bin positions, so the corresponding overhead remains bounded and doesn't alter the scaling of the transform-evaluation stage.

Here, K, R, and N denote the numbers of scanned frequency bins, scanned ROCOF bins, and time samples, respectively. Moreover, I_{NR} is the average number of NR iterations, where M_f and M_R denote the monomial counts of the frequency- and ROCOF-correction polynomials, respectively, and c_J is the constant cost associated with the construction and solution of the Jacobian system. Finally, M_ϕ^c, M_f^c, and M_R^c denote the monomial counts of the phase, frequency, and ROCOF compensation polynomials, respectively. As shown in Table II, the dominant term remains the transform evaluation, while NR, COI fusion, and bias compensation only introduce bounded post-processing overhead.

The Open-Source MATLAB code of the IpQPFT method discussed in the current article can be found in [31].

H. Computational Time Quantification

Since the proposed estimator is executed as a predominantly sequential routine, the Geekbench 6 single-core score was adopted as a processor-normalization indicator for the measured computational capability, where the test platform used in this work (Dell Latitude 3440, Intel Core i5-1345U) achieved a Geekbench 6 single-core score of 522 [32]. Despite no direct Raspberry Pi 5 execution-time quantification being performed in the present work, a Raspberry Pi 5 with a representative Geekbench 6 single-core score of approximately 900 [33] would provide higher sequential computational capability than the test platform considered here. This suggests that the same implementation could run faster on such a processor without a strict inverse-time scaling [34]. Therefore, this comparison is used only to contextualize the reported measurements and provide an approximate indication of the feasibility of porting the implementation to a Raspberry Pi 5. Moreover, the implementation was written and tested in high-level MATLAB code, rather than optimized low-level code such as C/C++ or an FPGA implementation, which generally provides lower and more deterministic processing latency than general-purpose CPU-based platforms [12], [26]. Based on the test conditions presented in Table III, the corresponding computational-time benchmark is reported in Table IV, where the proposed IpQPFT is compared with CSTFM and TLS-ESPRIT under the same computational conditions and on the same test platform. The revised results show that the proposed IpQPFT implementation requires 10.55±2.68 ms per estimation, compared with 43.03 ± 2.16 ms for CSTFM, and 171.26±22.84 ms for TLS-ESPRIT. Since the PMU reporting period is 20 ms, these results confirm that the proposed implementation is compatible with real-time operation at 50 fps, while the other analyzed methods exhibit higher computational costs.

TABLE IV
COMPUTATIONAL-TIME BENCHMARK OF THE ANALYZED ALGORITHMS OVER 981 EXECUTIONS

Algorithm	Mean [ms]	Std. dev. [ms]
IpQPFT	10.55	2.68
CSTFM	43.03	2.16
TLS-ESPRIT	171.26	22.84

V. CONCLUSION

This article presents the IpQPFT for the ROCOF-DFT, based on bi-dimensional polynomial interpolation and multivariate NR refinement. The proposed method acts as a ROCOF-aware enhancement of the IpDFT family, remaining fully compatible with conventional IpDFT procedures while improving the response under genuine frequency-ramp conditions. In particular, compared with CSTFM, the proposed estimator achieves substantially lower ramp-test error (i.e., 4 mHz/s) while also showing reduced variability under quasi-stationary and harmonic-distortion conditions.

The AM and PM tests highlighted the expected tradeoff between window length and modulation-tracking capability. The 10-cycle realization offers the best static and ramp performance, but its longer observation window averages out faster AM and PM components. On the other hand, the 5-cycle realization improves responsiveness and recovers compliance for the higher modulation cases, although at the expense of degraded static accuracy. Therefore, the observed AM and PM behavior is better interpreted as a time-resolution tradeoff than as a loss of estimator stability.

The real-case analysis based on the 2015 Turkey blackout further confirmed the practical behavior of the method. During the pre-contingency interval, the IpQPFT showed smoother performance under stable operating conditions, while during the disturbance, all methods tracked the event consistently and produced similar fault-related trends. In this scenario, the IpQPFT provided a window-consistent dynamic ROCOF estimate and also revealed sharp ROCOF transitions associated with the system separation.

From the implementation point of view, the method also remains attractive for real-time PMU applications, with a mean estimation time of 10.55 ms at 50 fps, confirming real-time feasibility previous to low-level optimization. Overall, the IpQPFT provides a practical compromise between dynamic ROCOF consistency, compatibility with IpDFT-based processing, and real-time computational feasibility.

Code Availability

The Open-Source MATLAB code is available in [31].

References

[1] G. Frigo, A. Derviškadić, Y. Zuo, and M. Paolone, "PMU-based ROCOF measurements: Uncertainty limits and metrological significance in power system applications," *IEEE Trans. Instrum. Meas.*, vol. 68, no. 10, pp. 3810–3822, Oct.2019.

[2] *IEEE/IEC International Standard—Measuring Relays and Protection Equipment—Part 118-1: Synchrophasor for Power Systems—Measurements*, Standard <pub-id pub-id-type="std-designation">IEC/IEEE 60255-118-1:2018</pub-id></std>, Dec.2018, pp. 1–78.

[3] L. Piotrowski, *Application of Phasor Measurement Units for Monitoring Power System Dynamic Performance*. CIGRE Technical Brochure, Paris, France, 2017.

[4] M. Chakir, I. Kamwa, and H. Le Huy, "Extended C37.118.1 PMU algorithms for joint tracking of fundamental and harmonic phasors in stressed power systems and microgrids," *IEEE Trans. Power Del.*, vol. 29, no. 3, pp. 1465–1480, Jun.2014.

[5] A. J. Roscoe, B. Dickerson, and K. E. Martin, "Filter design masks for C37.118.1a-compliant frequency-tracking and fixed-filter M-class phasor measurement units," *IEEE Trans. Instrum. Meas.*, vol. 64, no. 8, pp. 2096–2107, Aug.2015.

[6] A. Derviškadić, P. Romano, and M. Paolone, "Iterative-interpolated DFT for synchrophasor estimation in M-class compliant PMUs," in *Proc. IEEE Manchester PowerTech*, Jun. 2017, pp. 1–6.

[7] G. Frigo, P. A. Pegoraro, and S. Toscani, "Enhanced support recovery for PMU measurements based on Taylor–Fourier compressive sensing approach," *IEEE Trans. Instrum. Meas.*, vol. 71, pp. 1–11, 2022.

[8] A. Riepnieks and H. Kirkham, "Rate of change of frequency measurement," in *Proc. 57th Int. Sci. Conf. Power Electr. Eng. Riga Tech. Univ. (RTUCON)*, Oct. 2016, pp. 1–5.

[9] A. J. Roscoe, A. Dysko, B. Marshall, M. Lee, H. Kirkham, and G. Rietveld, "The case for redefinition of frequency and ROCOF to account for AC power system phase steps," in *Proc. IEEE Int. Workshop Appl. Meas. Power Syst. (AMPS)*, Sep. 2017, pp. 1–6.

[10] A. Karpilow, M. Paolone, A. Derviškadić, and G. Frigo, "Step change detection for improved ROCOF evaluation of power system waveforms," in *Proc. Int. Conf. Smart Grid Synchronized Meas. Analytics (SGSMA)*, May 2022, pp. 1–7.

[11] G. Frigo, D. Macii, and D. Petri, "Accuracy comparison of frequency and ROCOF dynamic estimators under contingencies," in *Proc. IEEE Int. Instrum. Meas. Technol. Conf. (I2MTC)*, Glasgow, U.K., May 2024, pp. 1–6.

[12] P. Banerjee, S. C. Srivastava, and A. K. Srivastava, "An improved method for estimating phasors and ROCOF suitable for M class PMUs," *IEEE Trans. Instrum. Meas.*, vol. 72, pp. 1–14, 2023.

[13] C. Cazal, G. Frigo, F. Ponci, and A. Monti, "The ROCOF-DFT: A discrete Fourier transform kernel adaptation for ROCOF tracking," in *Proc. IEEE 15th Int. Workshop Appl. Meas. Power Syst. (AMPS)*, Bucharest, Romania, Sep. 2025, pp. 1–6.

[14] L. P. Castro, M. R. Haque, M. M. Murshed, S. Saitoh, and N. M. Tuan, "Quadratic Fourier transforms," *Annals Funct. Anal.*, vol. 5, no. 1, pp. 10–23, 2014.

[15] L. P. Castro, L. T. Minh, and N. M. Tuan, "New convolutions for quadratic-phase Fourier integral operators and their applications," *Medit. J. Math.*, vol. 15, no. 1, p. 13, Feb.2018.

[16] C. Cazal, L. Tari, M. Ginocchi, F. Ponci, and A. Monti, "Ip-DFT based on polynomial interpolation and Newton-raphson: A multifrequency estimation alternative for zero-padding and window function independence," in *Proc. IEEE 14th Int. Workshop Appl. Meas. Power Syst. (AMPS)*, Sep. 2024, pp. 1–6.

[17] G. Frigo, A. Derviskadic, Y. Zuo, A. Bach, and M. Paolone, "Taylor-Fourier PMU on a real-time simulator: Design, implementation and characterization," in *Proc. IEEE Milan PowerTech*, Milan, Italy, Jun. 2019, pp. 1–6.

[18] C. A. Cazal et al., "A wideband zero-padded i-IpDFT algorithm for robust harmonic and interharmonic synchrophasor estimation," 2025, doi: 10.2139/ssrn.5686217.

[19] D. Kalman, "The generalized Vandermonde matrix," *Math. Mag.*, vol. 57, no. 1, pp. 15–21, Jan.1984.

[20] B. Mourrain and V. Y. Pan, "Multivariate polynomials, duality, and structured matrices," *J. Complex.*, vol. 16, no. 1, pp. 110–180, Mar.2000.

[21] S. Ly, K.-H. Pho, S.-H. Pan, and W.-K. Wong, "Newton-raphson method: Overview and applications," *Adv. Decis. Sci.*, vol. 28, no. 3, pp. 1–26, Sep.2024.

[22] R. A. Tapia, "The Kantorovich theorem for Newton's method," *Amer. Math. Monthly*, vol. 78, no. 4, pp. 389–392, 1971.

[23] A. Derviškadic, P. Romano, and M. Paolone, "Iterative-interpolated DFT for synchrophasor estimation: A single algorithm for P - and M-class compliant PMUs," *IEEE Trans. Instrum. Meas.*, vol. 67, no. 3, pp. 547–558, Mar.2018.

[24] L. N. Trefethen, *Approximation Theory and Approximation Practice, Extended Edition*. Philadelphia, PA, USA: SIAM, 2019.

[25] D. Macii, D. Belega, and D. Petri, "IpDFT-tuned estimation algorithms for PMUs: Overview and performance comparison," *Appl. Sci.*, vol. 11, no. 5, p. 2318, Mar.2021.

[26] P. Romano and M. Paolone, "Enhanced interpolated-DFT for synchrophasor estimation in FPGAs: Theory, implementation, and validation of a PMU prototype," *IEEE Trans. Instrum. Meas.*, vol. 63, no. 12, pp. 2824–2836, Dec.2014.

[27] S. Arridge, P. Maass, O. Öktem, and C.-B. Schönlieb, "Solving inverse problems using data-driven models," *Acta Numerica*, vol. 28, pp. 1–174, May2019.

[28] M. Bertocco, G. Frigo, C. Narduzzi, C. Muscas, and P. A. Pegoraro, "Compressive sensing of a Taylor-Fourier multifrequency model for synchrophasor estimation," *IEEE Trans. Instrum. Meas.*, vol. 64, no. 12, pp. 3274–3283, Dec.2015.

[29] Project Group Turkey, *Report on Blackout in Turkey on 31st March 2015—Final Version 1.0*, TE and ENTSO-E, Ankara, Turkey, Sep.2015.

[30] G. Frigo, P. A. Pegoraro, and S. Toscani, "Tracking power systems events: PMU, reporting rate, interpolation," in *Proc. Int. Conf. Smart Grid Synchronized Meas. Anal. (SGSMA)*, May 2022, pp. 1–6.

[31] C. Cazal. (2026)*IpQPFT on ROCOF-DFT · GitLab open source code*. [Online]. Available: https://gitlab.git.nrw/cesar.cazal/ipqpft-on-rocof-dft

[32] G. 6. (2026). *CPU Benchmark*. [Online]. Available: https://browser.geekbench.com/v6/cpu/17227056

[33] *Raspberry Pi 5 Model B Rev 1.1—Geekbench*. Accessed: Mar. 23, 2026. [Online]. Available: https://browser.geekbench.com/v6/cpu/18033066

[34] M. D. Hill and M. R. Marty, "Amdahl's law in the multicore era," *Computer*, vol. 41, no. 7, pp. 33–38, Jul.2008.

Cesar Cazal (Graduate Student Member, IEEE) received the Engineering degree (Hons.) in electronics from the Universidad Nacional de Asunción, San Lorenzo, Paraguay, in 2016, and the M.Sc. degree in electrical engineering with a major in power systems from RWTH Aachen University, Aachen, Germany, in 2019, where he is currently pursuing the Ph.D. degree with the E.ON Energy Research Center.

Guglielmo Frigo (Senior Member, IEEE) received the Ph.D. degree from the University of Padova, Padua, Italy, in 2015.

He was a Post-Doctoral Researcher with the University of Padova from 2015 to 2017 and with EPFL, Lausanne, Switzerland, from 2018 to 2020. In 2020, he was a Foreign Guest Researcher with NIST, Gaithersburg, MD, USA, and is currently a Senior Scientist with METAS, Bern, Switzerland. Since October 2025 has served as Convenor of IEC SC77A WG9, "Power quality measurement methods." His research interests include enhanced measurement infrastructures for electrical power systems.

Ian Andrés Morales Sandoval received the B.Sc. degree from RWTH Aachen University, Aachen, Germany, in 2025, where he is currently pursuing the master's degree in electrical engineering.

Currently working as a Student Research Assistant, with a focus on systems and automation.

Ferdinanda Ponci (Senior Member, IEEE) received the Ph.D. degree in electrical engineering from the Politecnico di Milano, Milan, Italy, in 2002.

She was an Assistant Professor at the University of South Carolina, Columbia, SC, USA, from 2003 and earned tenure in 2008. Since 2009, she has been a Professor at the E.ON Energy Research Center, RWTH Aachen University, Aachen, Germany, specializing in monitoring and distributed control of power systems.

Dr. Ponci serves on the IEEE Instrumentation and Measurement Society Administration Committee and is Liaison with IEEE Women in Engineering.

Antonello Monti (Senior Member, IEEE) received the M.Sc. (summa cum laude) and Ph.D. degrees in electrical engineering from the Politecnico di Milano, Milan, Italy, in 1989 and 1994, respectively.

He started his career at Ansaldo Industria, Milan, and then joined Politecnico di Milan as an Assistant Professor in 1995. In 2000, became an Associate Professor, then a Full Professor, at the University of South Carolina, Columbia, SC, USA. Since 2008, the Director of the E.ON Energy Research Center at RWTH Aachen University, Aachen, Germany.

Dr. Monti was the recipient of the 2017 IEEE Innovation in Societal Infrastructure Award. He is an Associate Editor of IEEE SYSTEMS JOURNAL and *IEEE Electrification Magazine*.